Design and Synthesis of Trithiophene-Bound Excited-State Intramolecular Proton Transfer Dye: Enhancement on the Performance of Bulk Heterojunction Solar Cells

Dong-Yi Chen,[†] Chyi-Lin Chen,[†] Yi-Ming Cheng,[†] Cheng-Hsuan Lai,[†] Jian-Yuan Yu,[†] Bo-So Chen,[†] Cheng-Chih Hsieh,[†] Hsieh-Chih Chen,[†] Li-Yin Chen,[‡] Ching-Yen Wei,[§] Chung-Chih Wu,[‡] and Pi-Tai Chou*[,†]

Department of Chemistry and Instrumentation Center and Graduate Institute of Photonic and Optoelectronics, National Taiwan University, Taipei 106, Taiwan, and Materials and Chemical Laboratories, Industrial Technology Research Institute, Hsinchu 310, Taiwan

ABSTRACT In an aim to harvest UV−near-visible (360−440 nm) photons as well as to increase the morphology in the bulk heterojunction solar cells, we report herein the strategic design, synthesis, and characterization of a novel excited-state intramolecular proton-transfer dye, 3-hydroxy-2-(5-(5-(5-(3-hydroxy-4-oxo-4H-chromen-2-yl)thiophen-2-yl)thiophen-2-yl)thiophen-2-yl)-4H-chromen-4-one (**FT**), which bears two key functional groups, namely 3-hydroxychromone chromophore and trithiophene backbone and is then exploited into the blends of regioregular poly(3-hexylthiophene) (**RR-P3HT**) and phenyl-C_{61}-butyric acid methyl ester (**PCBM**). **FT** acts as an excellent UV-near visible absorber, which then undergoes excited-state intramolecular proton transfer, giving rise to an orange-red proton-transfer emission that was reabsorbed by **P3HT** via a Förster type of energy transfer. Introduction of **FT** to **P3HT/PCBM** blend films also improves the morphology of phase separated structure, in particular, enhances the interaction of **P3HT** chains and the hole mobility. In this work, under the optimized condition of **P3HT**: **PCBM**:**FT** of 15:9:2 in weight ratio, the best performance of the device **B-FT2** revealed consistent enhancements in the efficiency (η) 4.28% and short-circuit current (J_{sc}) 12.53 mAcm^{-2}, which are higher than that (3.68% and 10.28 mAcm^{-2}) of the best performance of the control device **B** (**P3HT**:**PCBM** 15:9 in weight ratio) by 16 and 22%, respectively.

KEYWORDS: excited-state intramolecular proton transfer • flavone • bulk-heterojunction • solar cell

1. INTRODUCTION

Bulk heterojunction (**BHJ**) solar cells have attracted much attention because of their simplicity in processing, flexibility, and potentially low cost. Typical **BHJ** solar cells consist of a transparent tin-doped indium oxide bottom electrode, electron-blocking layer, usually poly(3,4-ethylenedioxythiophene)-poly(styrenesulfonate) (**PEDOT:PSS**), active layer composed of electron donor and acceptor and top electrode (LiF/Al). Despite numerous different **BHJ** configurations being reported (1−6), so far, the most common **BHJ** solar cell with high power conversion efficiencies (PCEs) should be credited to the device with an active layer consisting of a blend of electron donor regioregular poly(3-hexylthiophene) (**RR-P3HT**) and electron acceptor, the fullerene derivative [6,6]-phenyl-C61 butyric acid methyl ester (**PCBM**) that possesses an energetically deep-lying LUMO. In this configuration, **RR-P3HT** chains tend to stack into lamella structures normally oriented perpendicular to the substrate. Higher RR enables closer packing of these lamellae, which could be responsible for the red shoulder on the long-wavelength (∼600 nm) absorption and for the larger field-effect mobility (7).

In **BHJ** solar cells, strongly bound electron−hole pairs, i.e., excitons, formed after irradiation and may become free charge carriers only when they diffuse to the interface between electron donor and electron acceptor. To achieve better performance of the **BHJ** cells, the two components of the active layer should be phase-separated on decent distance within the extreme exciton diffusion length (∼10 nm), leading to an optimum interfacial area. On these bases, numerous attempts focusing on the morphology of nanoscale phase-separated domains have been made. One widespread method should be credited to the improvement of active layer via thermal, electrical, and solvent annealing (8), such that the free space and the density of defects can be reduced and thereby the photogenerated carriers as well as the mobility of charge carriers are increased. In yet another approach, the photovoltaic (PV) efficiency can also be improved by increasing the hole mobility of donor. A widely accepted method is to increase molecular weight and/or to decrease polydispersity of polymers (9), the result of which enhances the backbone $\pi-\pi$ stacking, producing highly

---

* Corresponding author. E-mail: chop@ntu.edu.tw. Tel: (886) 2-3366-3894. Fax: (886) 2-2369-5208.

Received for review February 11, 2010 and accepted May 14, 2010

[†] Department of Chemistry and Instrumentation Center, National Taiwan University.

[‡] Graduate Institute of Photonic and Optoelectronics, National Taiwan University.

[§] Industrial Technology Research Institute.

DOI: 10.1021/am100126y

Scheme 1. Synthetic Route of FT (compd 5); MOMCl = Chloro(methoxy)methane

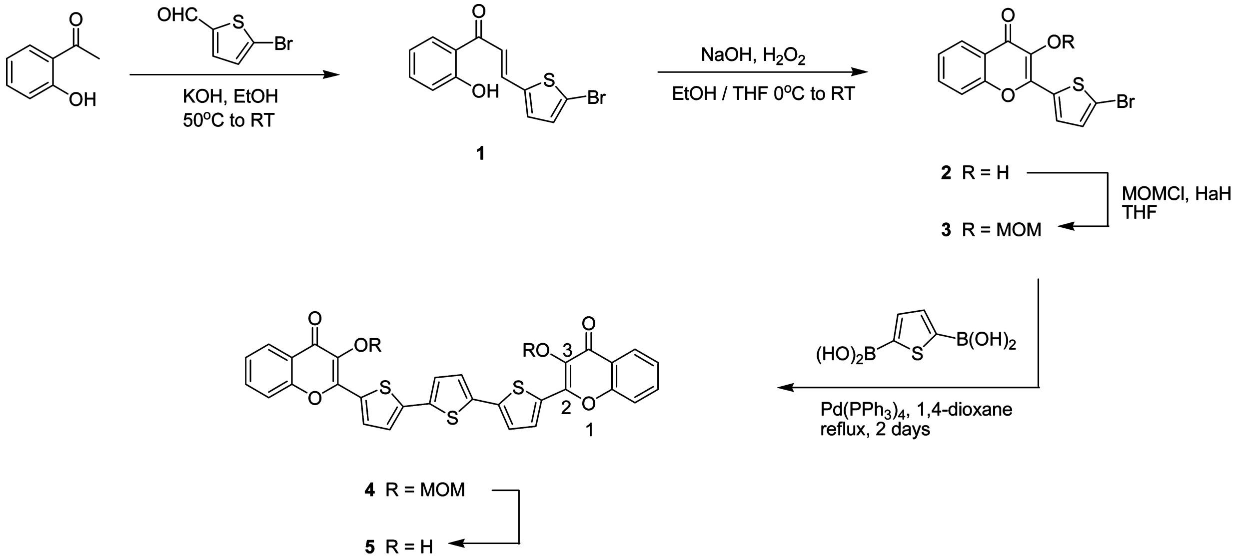

organized morphology by side chain self-assembly (10). Alternatively, via polymerization using a more rigid planar monomer, the morphology can be improved by forming a liquid-crystalline phase structure (11). Also, blends of active polymer with either conjugated (conducting or semiconducting) materials/polymer or small molecules may render good electrical properties by their matching structures and mechanical advantages (12). For the latter approach, we have recently reported the Cu^+ chelated poly alkoxythiophene (**P3MEET**) enhancement of a solar cell device consisting of a **P3HT/PCBM** heterojunction system. Compared to the reference **P3HT/PCBM** system, a consistent increase of conversion efficiency of 0.9% via apparent increase of IPCE is achieved upon optimizing the ratio of **P3MEET-Cu$^+$/P3HT/PCBM**. We conclude that match in redox potential and increase in ordering of the film upon doping **P3MEET-Cu$^+$** play two key roles for the enhancement.

The above polymer adduct, though being advantageous in morphology matching, unfortunately is not cost-effective in syntheses, and it is a nontrivial task for the precise size control (distribution of molecular weight). Alternatively, small organic molecules offer advantages regarding synthetic simplicity and versatility in modification. In this contribution, we plan to design small molecule and use it as adduct to enhance **BHJ** cells performance. Our goal of this project is aimed at two folds, namely to (1) perhaps enhance the morphology of **BHJ** active layer and 2. harvest UV and near visible (360−440 nm) photons, which are relatively inferior in energy conversion due to lower absorptivity and/or other radiationless deactivation to the ground state. For the latter approach, one feasible way is to utilize the mechanism of energy transfer, such that the designed molecules strongly absorb, for example, 360−440 nm photons, whereas the accompanied emission exhibits large Stokes shift with peak wavelength located ideally at ∼560 nm to achieve maximum overlap with the highest lying absorption of, for example, **P3HT**. Under this circumstance, efficient Förster type energy transfer may take place.

After screening numerous classes of molecules, it seems that those molecules undergoing excited-state intramolecular proton transfer (ESIPT) fulfill the requirement. The ESIPT reaction generally incorporates transfer of a hydroxyl (or amino) proton to the carbonyl oxygen (or pyridyl nitrogen) through a pre-existing hydrogen bonding configuration. Upon UV-near visible absorption, proton transfer usually takes place either coherently (13) or via the vibrational motions associated with hydrogen bond (14) within an ultrafast time scale. The resulting proton-transfer tautomer possesses significant differences in structure and electronic configuration from its corresponding normal species. Accordingly, a large Stokes shifted $S'_1 \rightarrow S'_0$ fluorescence (hereafter, the prime sign denotes the proton-transfer tautomer) was generally observed in the visible region (15, 16), which may be suited for above-mentioned energy transfer, fulfilling the goal of harvesting UV−near-visible solar energy.

We have thus examined the reported ESIPT molecules that met above criteria in an aim to enhance **BHJ** performance. Unfortunately, to our disappointment, none of the commercially available and/or literature reported ESIPT molecules worked for the **P3HT/PCBM BHJ** cells. To our experiences, incompatibility in morphology should account for the experimental failure (vide infra). Thus, strategic design of an ESIPT molecule, for which the structure is compatible to, for example the **P3HT** framework, should be of prime concern. Herein, we report the synthesis, characterization, and luminescence properties of a new excited-state intramolecular proton-transfer dye, 3-hydroxy-2-(5-(5-(5-(3-hydroxy-4-oxo-4H-chromen-2-yl)thiophen-2-yl)thiophen-2-yl)thiophen-2-yl)-4H-chromen-4-one (**FT**, see Scheme 1), bearing two key functional groups, 3-hydroxychromone as the UV−near-visible absorbing dye and trithiophene moiety to mimic backbone of **P3HT**, such that both spectral coverage of ESIPT emission and molecular structure fit well to the **P3HT/PCBM** system. As a result, consistently gaining photon harvesting and hence cell performance have been achieved.

2. EXPERIMENTAL SECTION

All reactions were performed under nitrogen. Solvents were distilled from appropriate drying agents prior to use. Commercially available reagents were used without further purification unless otherwise stated. All reactions were monitored by TLC with Merck precoated glass plates (0.20 mm with fluorescent indicator UV254) and were visualized with UV light irradiation at 254/366 nm. Flash column chromatography was carried out with use of silica gel from Merck (230−400 mesh). Mass spectra were obtained on a JEOL SX-102A instrument operating in electron impact (EI) or fast atom bombardment (FAB) mode. The ^{1}H and ^{13}C NMR spectra were obtained on Bruker spectrometers operating at frequencies as indicated for each compound. Chemical shifts were reported relative to $CDCl_3$ (1H 7.24) and at 77.0 ppm in $CDCl_3$ [^{13}C (central line of t)]. FT-IR spectra were recorded on a Nicolet magna-IR 550 series II. Melting points were uncorrected.

2.1. Syntheses. ***(E)-3-(5-Bromothiophen-2-yl)-1-(2-hydroxyphenyl)prop-2-en-1-one (1).*** KOH (2.9 equiv) was added to a suspension of relevant aldehyde (1.0 equiv) and the appropriate acetophenone (1.05 equiv) in EtOH (6 mL/mmol acetophenone). The mixture was stirred at 50 °C for 3 h, and then cooled to room temperature and kept there overnight. The reaction mixture was poured into water and acidified with aqueous HCl (1 M) to obtain the corresponding chalcone **1** that could be further crystallized in EtOH (yield:65%). Spectroscopic and analytical data: ^{1}H NMR (in $CDCl_3$): δ 12.73(s, 1H), 7.91−7.87(d, J=38, 1H), 7.83−7.80(m, 1H), 7.48−7.42(m, 1H), 7.32−7.28(m, 1H), 7.13−7.12(m, 1H), 7.05(1H), 7.01(m, 1H), 6.99−6.93(m, 1H).

2-(5-Bromothiophen-2-yl)-3-hydroxy-4H-chromen-4-one (2). Aqueous 30% H_2O_2 (8−11 equiv.) was added to a solution of the appropriate chalcone **1** (1.0 equiv.) and aqueous 4 M NaOH (5.0 equiv.) in a 1:1 mixture of MeOH and THF (20 mL/mmol chalcone) at 0 °C. The reaction was stirred at room temperature overnight. The resulting mixture was then acidified with aqueous HCl (1 M) and the product **2** was filtered off (yield: 40%). Spectroscopic and analytical data: ^{1}H NMR (in $CDCl_3$ solvent): δ 8.20−8.18 (d, J = 20, 1H), 7.71−7.67(m, 2H), 7.52−7.50(m, 1H), 7.38(m, 1H), 7.16−7.15(d, J = 10, 1H).

2-(5-Bromothiophen-2-yl)-3-(methoxymethoxy)-4H-chromen-4-one (3). Sodium hydride (60% in mineral oil) (0.72 g, 18.6 mmol) was washed with petroleum ether (10 × 3 mL). The gray powder was then suspended in THF (50 mL) and cooled to 0 °C. Compound **2** (0.72 g, 2 mmol) was then added dropwise and the solution was allowed to stir for 0.5 h. Chloromethyl methyl ether (0.49 g, 6 mmol) was added, and after 0.75 h, the reaction mixture was warmed to room temperature and stirred for 12 h. The reaction mixture was then concentrated, acidified with saturated aqueous ammonium chloride (25 mL), and extracted with ethyl acetate (2 × 40 mL). The organic layers were combined, dried ($MgSO_4$), and concentrated in vacuo to obtain **3** (yield:70%). Spectroscopic and analytical data:^{1}H NMR: δ 8.14−8.12(d, J = 20, 1H), 7.66−7.65(m, 1H), 7.62−7.57(m, 1H), 7.42−7.40(m, 1H), 7.33−7.29(m, 1H), 7.10−7.09(m, 1H), 5.49(s, 2H), 3.50(s, 3H). ^{13}C NMR δ 172.8, 153.8, 149.3, 134.5, 133.0, 132.3, 129.8, 125.2, 124.3, 123.5, 119.1, 117.1, 97.0, 85.5.

3-Hydroxy-2-(5-(5-(5-(3-hydroxy-4-oxo-4H-chromen-2-yl)thiophen-2-yl)thiophen-2-yl)thiophen-2-yl)-4H-chromen-4-one (5, FT). A mixture of compound **3** (1.46 g, 4.06 mmol), 2,5-thiophenediboronic acid (0.27 g, 1.60 mmol), $Pd(PPh_3)_4$ (0.17 g, 0.15 mmol), and 2 M Na_2CO_3 aqueous solution (17 mL, 34 mmol) in THF (25 mL) was degassed with N_2 for 5 min. The reaction mixture was stirred at reflux temperature under N_2 for 18 h. After being cooled to room temperature, water (50 mL) was added and extracted with CH_2Cl_2 (50 mL × 2). The combined organic phases were washed with water (50 mL), and brine solution (50 mL), dried over anhydrous Na_2SO_4, filtered, and the solvents were removed to dryness. Purification by column chromatography over silica gel eluting with a mixture of CH_2Cl_2 and hexane (1:4), followed by recrystallization from a mixture of CH_2Cl_2 and methanol, afforded yellow solids **5** (78%). Spectroscopic and analytical data: ^{1}H NMR δ 8.18−8.15(m, 2H), 7.63−7.57(m, 4H), 7.47−7.44(m, 2H), 7.34−7.31(m, 2H), 7.27−7.25(m, 2H), 7.19−7.15(m, 2H).The OH peak was not observed. ^{13}C NMR δ 173.5, 154.4, 151.2, 142.8, 136.2, 135.0, 133.1, 130.7, 129.7, 127.9, 127.3, 125.6, 124.6, 123.8, 117.5. EI-MS(MH^+): 569.33. Elemental anal. Calcd: C, 63.37; H, 2.84; O, 16.88; Found: C, 63.31, H, 2..88, O, 16.84.

2.2. Spectroscopic and Dynamic Measurements. Steady-state absorption and emission spectra were recorded by a Hitachi (U-3310) spectrophotometer and an Edinburgh (FS920) fluorimeter, respectively. Detailed lifetime measurement has been described in the previous report (17). Briefly, the fundamental pulses (750−840 nm) of a femtosecond Ti:Sapphire oscillator (80 MHz, Spectra Physics) was used to produce second harmonic (375−420 nm) as an excitation light source. Pico-nanosecond lifetime was measured with a time-correlated single photon counting system (Edinburgh OB 900 L), the resolution of which is limited by the detector response of ∼120 ps. The fluorescence decays were analyzed by the sum of exponential functions with an iterative convolution method, which allows partial removal of the instrument time broadening and consequently renders a temporal resolution of ∼80 ps

2.3. Device Properties and Measurement. The photovoltaic cells were fabricated by spin-coating. Polymer/PCBM blend is dissolved in chlorobenzene. Polymeric bulk-heterojunction solar cells (glass/ITO/PEDOT:PSS/P3HT:PCBM/LiF/Al) were fabricated using a method similar to that in the previous report (18). As for the solar cell performance, five devices have been fabricated for optimizing the photoelectric characters of the active-layered films by adding various amount of **FT**. (from 0 to 6 mg) These five devices specified as **B**, **B-FT1** (1 mg), **B-FT2** (2 mg), **B-FT4** (4 mg), and **B-FT6** (6 mg) were prepared with the same **P3HT**:**PCBM** weight ratio of 10:6 (**P3HT** 15 mg in 1 mL chlorobenzene), a typical format for making the corresponding **P3HT**/**PCBM** solar cells. The organic photovoltaic devices of polythiophene/fullerene-based **BHJ** solar cell embrace anode/active layer/cathode. The anode was composed of a modified poly(3,4-ethylenedioxythiophene): poly(styrene sulfonate) (PEDOT:PSS) layer (ca. 30 nm) deposited by spin-coating on the transparent electrode of glass substrate coated with indium−tin oxide (ITO). The glass substrates of transparent conducting electrode were carefully cleaned in an ultrasonic bath with detergent, deionized water, acetone, and ethanol, and dried in oven by turns. The substrates were further cleaned with ultraviolet ozone for 15 min. The formulas with varied **FT** weight were prepared by magnetically stirring for 48 h and then filtered using 0.2 μm syringe filters in the glovebox at N_2 atmosphere ($O_2 < 0.1$ ppm, $H_2O < 0.1$ ppm). The active layers of polymer photovoltaic devices were fabricated also in the glovebox by spin-coating (1500 rpm, for 60s) the blends on a cleaned ITO substrate spin coated with PEDOT:PSS. The cathode consisting of LiF (ca. 0.5 nm)/Al (ca. 100 nm) was thermally evaporated through a shadow mask to define the active area of the devices (0.04 cm^2). Finally, the ITO/PEDOT:PSS/active layer/LiF/Al devices were sealed with groove etched glasses by UV-cured mucilage.

Light-to-electricity conversion efficiency values were measured using a standard AM1.5 solar simulator-Oriel 66 924 Arc lamp source with a 6266 450 W Xe lamp, coupled with a Oriel 81088 Air Mass 1.5 Global Filter and the $I-V$ curves were measured by using a Keithley 2400 sourcemeter. The incident light intensity was calibrated by using a standard solar cell composed of a crystalline silicon solar cell and an IR cutoff filter (Schott, KG-5), giving the photoresponse range similar to that of amorphous silicon solar cell.

Scheme 2. Molecular Structure of FT and Its Intramolecular Proton Transfer Process in the Excited State

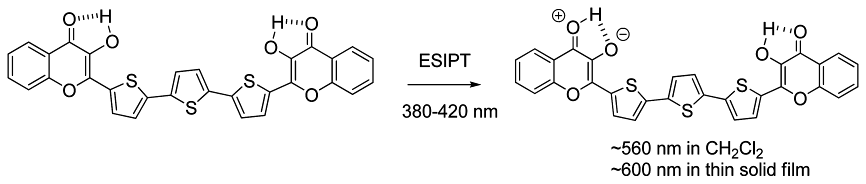

The morphology of the active layers was measured by using TM-AFM (tapping mode atomic force microscopy) and c-AFM (conductive-AFM) with a NanoScope IIIa controller (Veeco Metrology Group/Digital Instruments, Santa Barbara, CA). TM-AFM images were acquired using a 10-μm scanner and monolithic silicon cantilevers (NCHR, NanoWorld, Neuchatel, Switzerland), for which the force constant, scanning speed, and the typical tip radius of curvature were 42 nN/m, 1 Hz and 10 nm, respectively. The c-AFM measurements used Platinum/iridium cantilevers tip (EFM, NanoWorld, Neuchatel, Switzerland) with force constants of 2.8 N/m and resonance frequencies of 75 kHz. The force was constantly monitored and set at 2.5 nN. The microscope was housed in a Plexiglas chamber, through which dry N_2 was purged throughout the experiments, and the humidity was kept lower than 2%.

The information of carrier transport in organic films can be derived from the profile of the transient photocurrent signal measured by TOF technique. The TOF samples were prepared by sandwiching the organic thin film between two blocking contacts (e.g., Al/organic thin film/Al), with at least one contact to be transparent or semitransparent for illumination. Organic thin films were prepared by dip-casting the blend (P3HT-PCBM-FT) in chlorobenzene on the semitransparent substrate, which was thermally coated with Al and dried under vacuum. The top-contact Al was also deposited by thermal coating under vacuum (1×10^{-6} Torr). A third harmonic of a Nd:YAG laser was used to generate the excitation pulse ($\lambda = 355$ nm).

3. RESULTS AND DISCUSSION

3.1. Design and Synthetic Strategy.

Compound **FT** is composed of two functionalized groups, i.e., di-3-hydroxychromone and trithiophene moieties linked at C(2) position (see Scheme 1), in which the parent 3-hydroxychrome (3HC) is featured with an $S_0 \rightarrow S_1$ absorption maximum at 355 nm. Upon excitation, ultrafast ($\ll$1 ps) ESIPT takes place in the 3-HC moiety, i.e. from the hydroxyl proton to the carbonyl oxygen, resulting in a proton transfer emission at ~520 nm (see Scheme 2 for **FT**) (19). Our design strategy lies in two folds. On the one hand, we expect that replacing the phenyl ring by trithiophene at the C(2) position, because of the elongation of the π conjugation, should further shift the absorption to the desired UV-near visible region, and hence its emission is expected to overlap with **P3HT** absorption, facilitating, for example, the Förster type energy transfer process. Note that dual 3HC chromophores are applied to doubly increase the absorptivity (c.f. single 3HC), and hence the absorption extinction coefficient. On the other hand, the framework of trithiophene is strategically designed to mimic the backbone of **P3HT**, such that the morphology between **FT** and **P3HT** could be compatible (vide infra).

Scheme 1 depicts the synthetic process for **FT**, in which the first step involved the formation of corresponding chalcone via condensation of commercially available 5-bromothiophene-2-carbaldehyde with *o*-hydroxy acetophenone in basified methanol solution. The resulting chalcone salt was neutralized, and the precipitate was filtered, washed with methanol and dried, rendering (*E*)-3-(5-bromothiophen-2-yl)-1-(2-hydroxyphenyl)prop-2-en-1-one, **1**, which then underwent an oxidative cyclization, forming the corresponding chromone, **2**. Protection of the hydroxyl group by chloro(methoxy)methane (MOMCl) furnished compound **3**. Suzuki coupling of **3** with thiophene-2,5-diyldiboronic acid proceeded smoothly to give **4**, which was then deprotected to obtain the desired product **FT 5**. Details of each synthetic procedure as well as characterization are elaborated in the experimental section.

3.2. Spectroscopy and Dynamics.

As shown in Figure 1, **FT** in cyclohexane (~2×10^{-5} M) exhibits UV−vis absorption spectrum with the lowest lying transition maximized at 360 nm in cyclohexane. The absorption extinction coefficient of 8.3×10^4 M^{-1} cm^{-1} at 360 nm warrants the $S_0 \rightarrow S_1$ to be an allowed $\pi-\pi^*$ transition. Upon electronic excitation (e.g., 360 nm), an anomalously large Stokes shifted yellow-orange emission maximum at 556 nm was resolved. When monitoring the emission band throughout 520−700 nm, the corresponding excitation spectra are all identical, which are also similar to the absorption spectrum, eliminating the possibility that the emission originates from any possible existence of **FT** isomer(s) as well as from any trace impurity. It is thus reasonable to assign the yellow-orange emission, with a Stokes shift of as large as ~9700 cm^{-1} (peak (absorption)-to-peak (emission)), to the fluorescence resulting from the excited-state intramolecular proton transfer (ESIPT) reaction (see Scheme 2). The decay time of the 556 nm proton-transfer emission was measured to be 4.7 ns, whereas the corresponding rise time was beyond system response limit of $\ll$80 ps. It is thus reasonable to

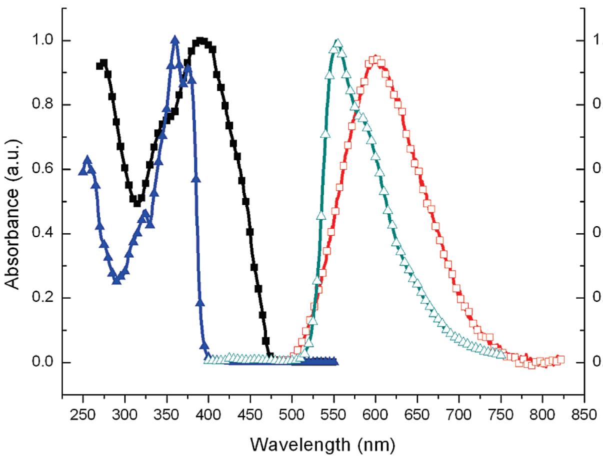

FIGURE 1. Absorption and emission of FT in cyclohexane (triangle) and solid film (square). Solid film is prepared by spin coating FT (dissolved in $CHCl_3$) on the quartz plate. $\lambda_{ex} \approx 365$ nm.

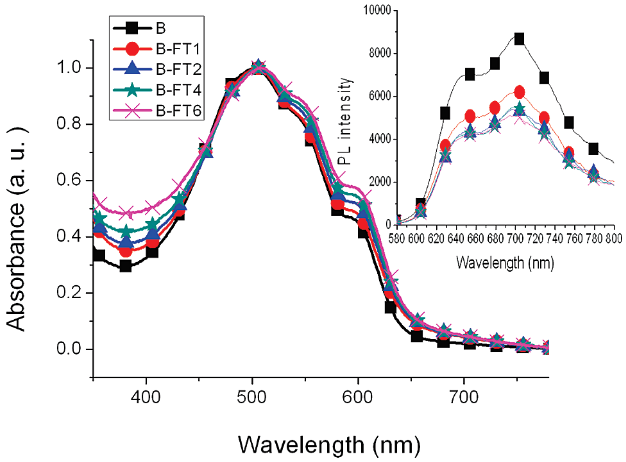

FIGURE 2. Absorption and PL (inset) spectra of 130−140 nm thick-blending film after annealing at 150 °C for 10 min. Solid square, circle, triangle, star, and cross symbols represent weight ratio of P3HT:PCBM:FT 15:9:0 (B), 15:9:1 (B-FT1), 15:9:2 (B-FT2), 15:9:4 (B-FT4), and 15:9:6 (B-FT6).

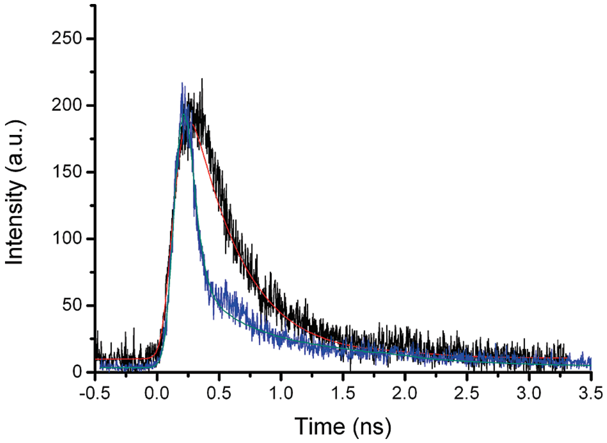

FIGURE 3. Time-dependent fluorescence decay dynamics of FT (black) and B-FT2 (blue) in the solid thin film monitored at 580 nm. FT, $\tau_f = 630$ ps; BFT-2, $\tau_{f1} < 80$ ps (82%) and $\tau_{f2} \approx 650$ ps (18%); $\lambda_{ex} = 350$ nm.

propose an ultrafast rate of ESIPT, resulting in a unique proton transfer tautomer emission. Assuming a unity efficiency of ESIPT, the quantum yield of **FT** in cyclohexane was then determined to be 0.35.

Figure 1 also depicts the absorption and emission spectra of **FT** in solid film that is prepared by spin coating **FT** (dissolved in $CHCl_3$) on the quartz plate. In comparison to **FT** in solution, the solid film absorption spectrum of **FT** exhibits an appreciable red shift of the peak wavelength to ~390 nm, accompanied with the appearance of a shoulder at ~440 nm. Comparing the respective random orientation of thiophene moieties in solution at RT, the rigidity of **FT** solid film may lean toward more coplanarity among trithiophenes and/or between thiophene and 3-hydroxychromone, resulting in the elongation of π-conjugation. At this stage, we also cannot rule out the role of the $\pi-\pi$ stacking, in part, to account for the spectral shift. Nonetheless, highly efficient ESIPT in **FT** still takes place in thin film, as evidenced by the unique emission band maximized at 600 nm ($\tau_f \approx 0.63$ ns), giving a peak-to-peak Stokes shift of ~8975 cm^{-1}.

Figure 2 illustrates the effect of adding **FT** on the absorption and emission properties of **P3HT**-**PCBM** blending film (**P3HT**:**PCBM**:**FT** in weight ratio, **B** (15:9:0), **B-FT1** (15:9:1), **B-FT2** (15:9:2), **B-FT4** (15:9:4), **B-FT6** (15:9:6). As shown in Figure 2, it is obvious that the ratio for absorptivity at >600 nm versus that at the peak wavelength 530 nm increases as the amount of **FT** added into the control device **B** increases, with a tendency of **B-FT1** (1 mg) > **B-FT2** (2 mg) > **B-FT4** (4 mg) ~ **B-FT6** (6 mg). Because **FT** has negligible absorptivity at >500 nm (see Figure 1), the increase of absorptivity at >600 nm, in theory, should be ascribed to that of **P3HT**-**PCBM** components. Moreover, similar enhancement of >600 nm absorption was also observed upon addition of **FT** to the pure **P3HT** film (see Figure S1 in the Supporting Information), supporting the interaction between **FT** and **P3HT.**

As for **P3HT**, the degree of regioregularity (**RR**), defined as the percentage of monomers adopting a head-to-tail configuration (20), has been known to affect both the optical properties and the properties of free charge-carriers of **RR-P3HT**. Brown et al. (21) recently concluded that the long-wavelength absorption band of **RR-P3HT** at ~600 nm could be ascribed to the interchain interactions. In this sense, upon addition of **FT**, the changes of absorption spectrum of **RR-P3HT** at >600 nm imply that **FT** plays certain role in assisting the interaction among the conjugated polymers. One conceivable mechanism is via the $\pi-\pi$ stacking interaction between the phenyl and thienyl moieties of **FT** and **RR-P3HT**. Note that there is also an appreciable increase of the absorption in the region of 360−440 nm. Although the possibility of changes of the environment around the polymers and/or the extent of polymer's aggregation in the blue region cannot be discarded, later results on energy transfer and device performance (vide infra) lead us to conclude that the enhancement mainly results from the absorption of **FT**.

The relaxation dynamics of **FT** in both pure and blended solid films was then performed in an aim to support the proposed energy transfer between **FT** and **P3HT**. As shown in Figure 3, sharp differences are readily distinguished between pure **FT** and blending **P3HT-PCBM-FT** film. In the case of pure **FT** in the solid film, upon monitored at the tautomer emission region (e.g., 580 nm), the decay curve was composed of a single exponential component, which is fitted to be around 0.63 ns. Conversely, when applied as a dopant such as in e.g. **B-FT2** film, as shown in Figure 3, the **FT** proton-transfer tautomer emission monitored at 580 nm exhibits multiexponential relaxation dynamics. Using a two-single-exponential decay components fitting procedure, the results consist of a system-response-limit decay (<80 ps) and a much longer component of ~0.65 ns that is consistent with the population decay time constant (~0.63 ns) of the pure **FT** film within experimental error. The fast, irresolvable (<80 ps) decay component implies that mixing of **FT** with **P3HT** and **PCBM** generates a fast nonradiative relaxation for **FT** in the excited state. We also performed **FT** relaxation dynamics in pure **P3HT** with the same ratio (by weight) as that in **B-FT2** device but without the presence of **PCBM**. The results also reveal dual decay components with the same fitted decay time constants (i.e., < 80 ps and ~630 ps, see

Figure S2 in the Supporting Information). The result clearly indicates that the major deactivation channel of **FT** proton-transfer tautomer emission is through the interaction with **P3HT**, whereas **PCBM** plays a minor part. Since the proton-transfer emission of **FT** strongly overlaps with the absorption spectrum of **P3HT** (see Figures 1 and 2), we thus propose that efficient Förster type energy transfer is operative from **FT** to **P3HT** in the blend solid film. Nevertheless, as evidenced by the long decay component being ascribed to the **FT** proton-transfer tautomer emission free from energy transfer, certain percentage of **FT** might be located far distance away from **P3HT** chromophore or at awkward orientation that energy transfer does not take place. At this stage, we unfortunately have no clue regarding the specific sites for executing or prohibiting energy transfer. Nonetheless, assuming the same radiative decay rate constant for **FT** proton-transfer tautomer emission in different environment, the ratio of the pre-exponential factor, i.e., the intensity at $t \approx 0$ ($I_t = 0$), for fast (<80 ps) versus slow (650 ps) components can be exploited to estimated the % of **FT** undergoing energy transfer, which is defined as Φ_{eff} and can be expressed below.

$$\Phi_{\text{eff}} = \frac{I_{t=0}^{\text{fast}}}{I_{t=0}^{\text{fast}} + I_{t=0}^{\text{slow}}}$$

As a result, Φ_{eff} is calculated to be ~82% in the **B-FT2** film. Note that this derivation assumes that energy transfer efficiency is near unity, as supported by its system-response-limited reaction time scale.

To further investigate the effect of **FT** on the exciton dissociation in the active-layered film, we also acquired photoluminescence (PL) spectra of **P3HT** for each device, and the results are depicted in inset of Figure 2. Upon excitation at, for example, 520 nm, where **FT** has negligible absorption, the PL intensity is mainly attributed to **P3HT** and is decreased in the order of **B** > **B-FT1** > **B-FT2** and then remains unchanged when **FT** added is more than 2 mg (see **B-FT4** and **B-FT6**). In good correlation with the absorption spectra, this result can be explained by the changes of morphology of the film. The results are consistent with the conclusion made by Korovyanko et al. (22), who reported a red-shifted absorption and lower quantum yield for more regioregular **P3HT** ($\Phi = 0.5\%$) as compared to that of regiorandom **P3HT** ($\Phi = 8\%$). In yet another approach, Brédas and co-workers (23) also reported that more self-assembled **RR-P3HT** (lamellae) exhibited stronger interchain interactions. Standing on these viewpoints, it clearly implies that **FT** could be an aid to **RR-P3HT** for exciton dissociation and charge transfer by enhancing the interaction between polymers. We will provide additional confirmation of this proposal in the following section of device performance.

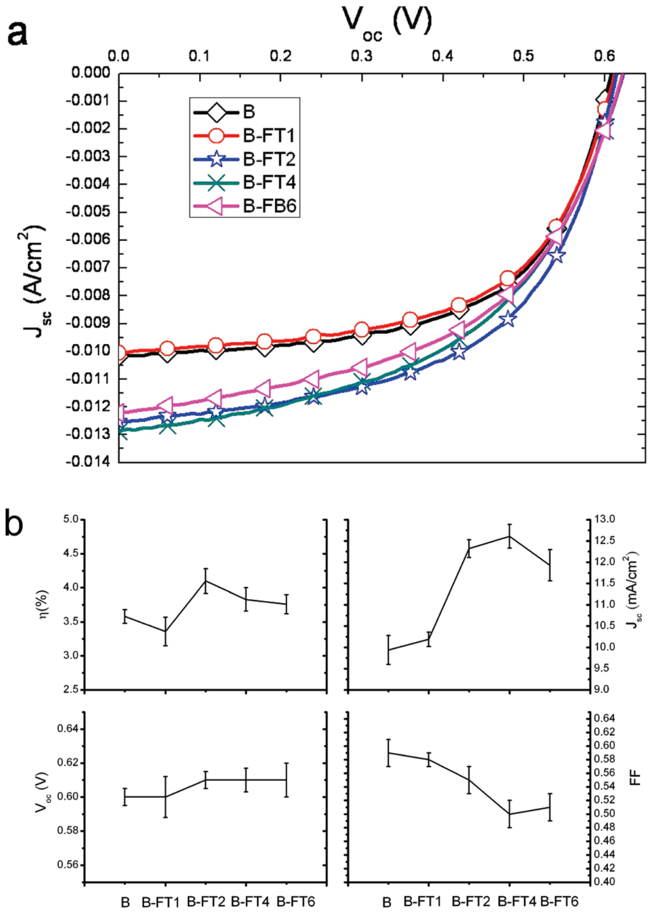

FIGURE 4. (a) *I*−*V* curves of photovoltaic devices with variant formulas. (b) Device parameters derived from five devices with various weight of FT.

3.3. Device Properties. Panels a and b in Figure 4a show the current−voltage (*J*−*V*) curves and the parameters of all the prepared devices **B**, **B-FT1**, **B-FT2**, **B-FT4**, and **B-FT6**. On the basis of three replica, the average power conversion efficiencies (η (%)) for **B**, **B-FT1**, **B-FT2**, **B-FT4**, and **B-FT6** were measured to be 3.58 ± 0.10%, 3.36 ± 0.21%, 4.10 ± 0.18%, 3.83 ± 0.17%, and 3.76 ± 0.14%, with the average current densities J_{sc} of 9.94 ± 0.34 mA cm^{-2}, 10.19 ± 0.17 mA cm^{-2}, 12.32 ± 0.21 mA cm^{-2}, 12.61 ± 0.28 (mA cm^{-2}, and 11.93 ± 0.37 mA cm^{-2}, respectively. The average open-circuit voltages (V_{oc}) were measured as 0.60 ± 0.005 V (**B**), 0.60 ± 0.012 V (**B-FT1**), 0.61 ± 0.005 V (**B-FT2**), 0.61 ± 0.007 V (**B-FT4**), and 0.61 ± 0.011 V (**B-FT6**). Accordingly, the average filled factors (FF) for **B**, **B-FT1**, **B-FT2**, **B-FT4**, and **B-FT6** were then calculated as 0.59 ± 0.02, 0.58 ± 0.01, 0.55 ± 0.02, 0.50 ± 0.02, and 0.51 ± 0.02, respectively. Among various devices, **B-FT2** reveals the best power conversion efficiency (η (%)) of 4.28% and the highest J_{sc} of 12.53 mA cm^{-2}, comparing the optimized efficiency of 3.68% and the optimized J_{sc} of 10.28 mA cm^{-2} in this study for **B** (with absence of **FT**).

Obviously, there is a consistent enhancement of device performance in J_{sc} and V_{oc} with addition of **FT** into the control device (**B**). As for J_{sc}, the result can be rationalized by the fact that the trend of increase in J_{sc} accords with the enhancement and broadening of absorption spectra near 400 and 600 nm in the range of visible light. On the other hand, the increase of V_{OC} in devices **B-FT1**, **B-FT2**, **B-FT4**, and **B-FT6** seems contradicting to the ordering of interchain, which in theory should increase HOMO of **P3HT** and hence decrease the V_{OC} (24). As for a tentative explanation, al-

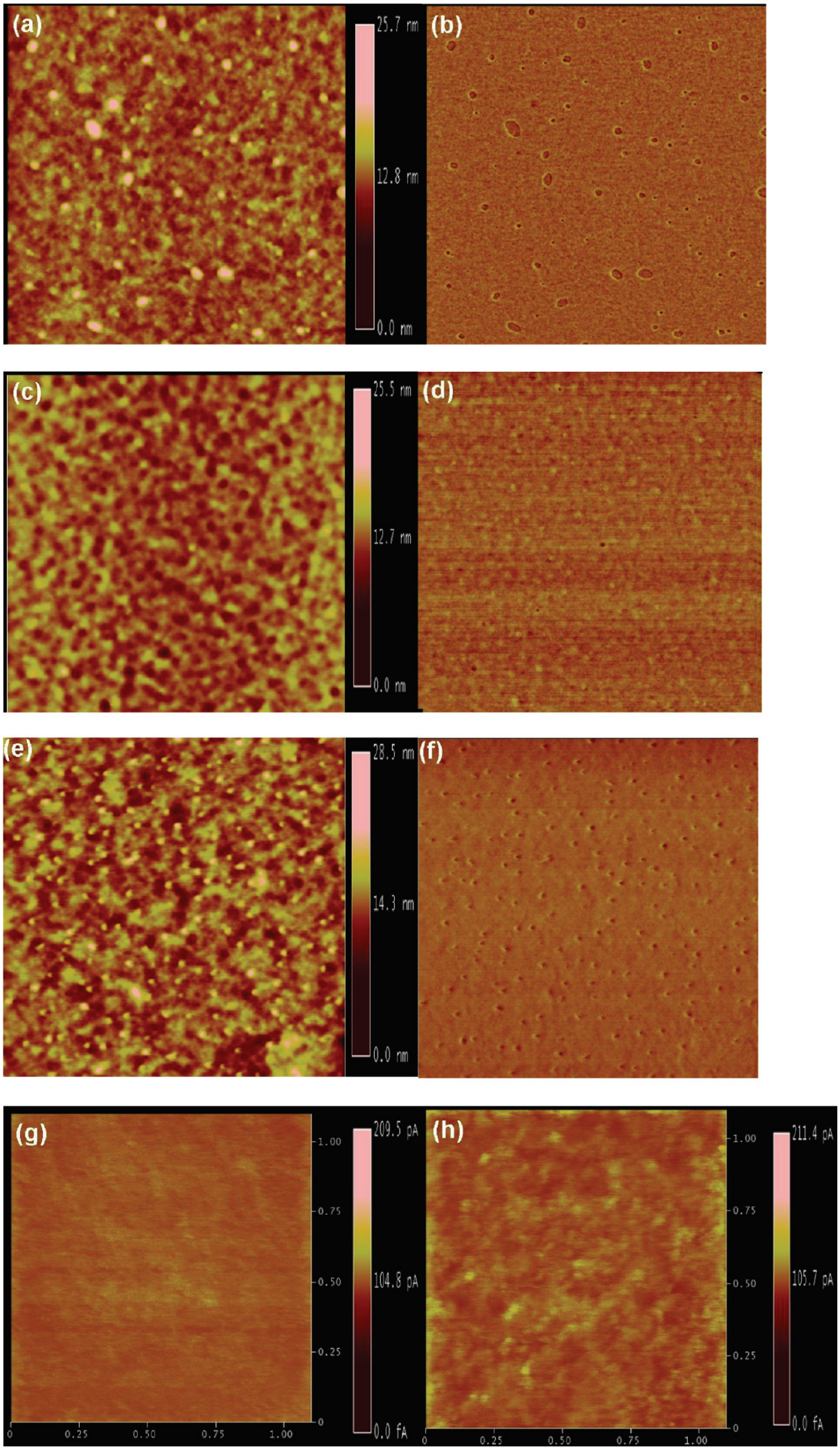

FIGURE 5. Tapping mode AFM topography and phase image of PV devices cast from (a, b) B device, (c, d) B-FT2, and (e, f) B-FT6, as well as C-AFM image of PV devices of (h) B-FT2 and (g) B.

though interaction between **FT** and **RR-P3HT** induces the ordering of interchains, the inset of **FT** into **RR-P3HT** seems to reduce the domain size of long-range ordering, such that the net effect is to decrease the HOMO energy level of **RR-P3HT**, giving rise to an increase in V_{OC}. Although direct support of this viewpoint is pending, indirect evidence is given by the AFM results shown in Figure 5. As shown in Figure 5b, AFM results clearly show that **PCBM** tends to aggregate and forms clusters after annealing because of the immiscibility between **P3HT** and **PCBM**. The addition of **FT**

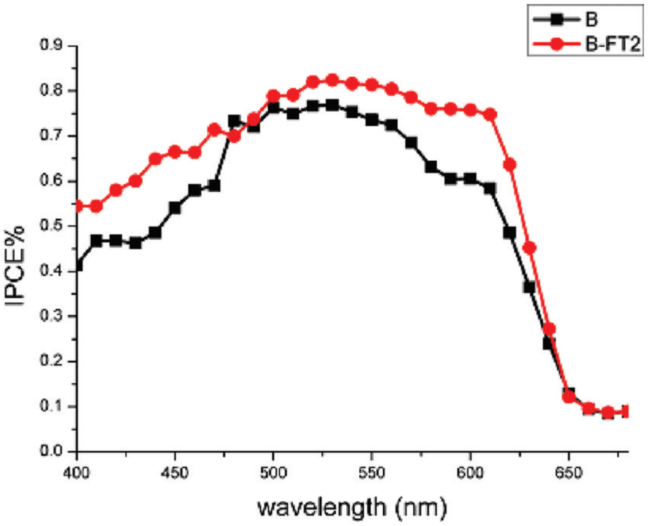

FIGURE 6. IPCE of devices, B and B-FT2, at wavelengths between 400 and 650 nm.

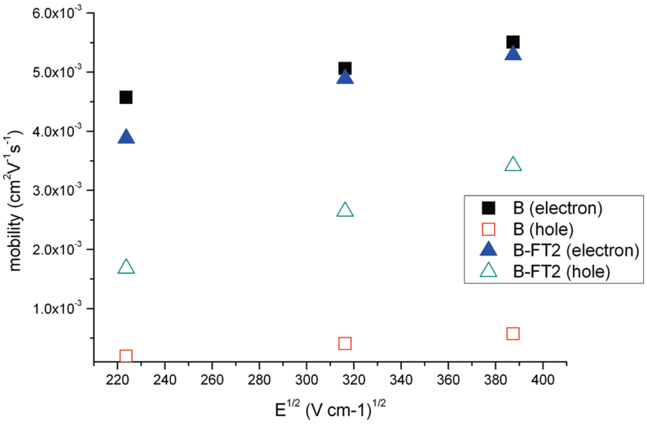

FIGURE 7. Electrical dependence of electron and hole mobility of devices B and B-FT2. Solid square and solid triangle are the electron mobility of B and B-FT2, respectively. Open square and open triangle are the hole mobility of B and B-FT2, respectively.

then acts as a mediator, which tends to reduce the aggregation formed by both **P3HT** and **PCBM**, as evidenced by the disappearance of the large clusters revealed in Figure 5d. Consequently, the prepared film (e.g., **B-FT2**) seems to be more homogeneous with the presence of smaller domains of aggregation, leading to larger surface area of phase separation.

Figure 6 depicts the incident photon-to-electron conversion efficiency (IPCE) spectra of two protocols, devices **B** and **B-FT2**. In comparison to that of control device **B**, it is clear that the enhancement of **IPCE** in **B-FT2** is mainly in two ranges, namely 400−440 nm via energy transfer mechanism and 600−650 nm via interchains enhancement. These two regions are qualitatively in agreement with the differences in absorption profile between **B** and **B-FT2** (vide supra). We further made an estimation on the contribution of each region for the enhancement. Assuming all solar photons in the range of 360−440 nm have been converted to electricity, J_{SC} is calculated to be 3.5 mAcm^{-2}. In comparison to the control device **B** we then calculate a 20% enhancement, for example, for device **B-FT2** according to the results of IPCE. Therefore, the increase in J_{SC} for **B-FT2** in the region of 360−440 nm is calculated to be 0.70 mAcm^{-2}. On the other hand, using the same method, the increase of J_{SC} for **B-FT2** in the region of 520−650 nm is calculated to be 1.68 mA cm^{-2}. Therefore, the contribution of 360−440 nm absorption to the overall increase (2.38 mA cm^{-2}) of the J_{SC} (c.f. device **B**) is more than 29%.

In addition to the enhancement of IPCE by the increase in absorptivity, we have reasons to believe that adding proton transferring dye, **FT**, could also provide good electronic communication between **P3HT** and **PCBM**. When the active layer is prepared through annealing processes, small molecule like **FT** might tend to insert into the space between **P3HT** and **PCBM** plausibly due to the interaction of the trithiophene and/or the phenyl groups with their analogous structure. This viewpoint may be supported by the C-AFM measurement. Images g and h in Figure 5 unveil how **FT** influences the electric property of the prepared device, e.g., conductivity. Under identical experimental condition, i.e., the same applied electric field, C-AFM results on the **B-FT2** film show apparently larger current density than that of **B** (current flows are shown by white spots in images g and h in Figure 5). Thus, the addition of **FT** in the blends may efficiently decrease the resistance of the active layer in the direction perpendicular to the substrate. Note that when the weight of **FT** surmounts 2 mg (i.e., 7.7% in weight), **FT** starts to precipitate because of its immiscibility in blending films (**P3HT-PCBM**) (see Figure 5f for **B-FT6**).

To assert enhancement of photocurrent in, for example, **B-FT2** being attributed to the improvement of carrier transport, the charge transport in the control device, **B**, as well **B-FT2** had been studied using the method of time-of-flight (TOF). The drift mobilityμ at an applied electric field E is deduced according to $\mu = d/Et_{tr}$, where d is the thickness of the film and t_{tr} is the transit time for the arrival of carriers at the collecting electrode. Figure 7 shows the field dependence of hole and electron mobility of the devices **B** and **B-FT2**. The mobility data are plotted as a function of the square root of applied electric field (E) according to the Poole-Frenkel relation of $\ln \mu = sE^{1/2}$, where s is the slope parameter. The electron mobilities μ_e for the devices **B** and **B-FT2** are evaluated to be 5.02×10^{-3} cm^2 V^{-1} s^{-1} and 4.89×10^{-3} cm^2 V^{-1} s^{-1} at $E = 1 \times 10^5$ V cm^{-1}, respectively. The calculated hole mobilities μ_h for the devices **B** and **B-FT2** are 4.11×10^{-4} cm^2 V^{-1} s^{-1} and 2.65×10^{-3} cm^2 V^{-1} s^{-1} at $E = 1 \times 10^5$ V cm^{-1}, respectively. Clearly, comparing device **B**, although the electron mobility remains similar, the hole mobility of the **B-FT2** device increases by almost 1 order of magnitude, leading to a more balanced charge transport when adding **FT** into the device **B** to make the device **B-FT2**. With the increase in the hole transportation, the device recovers from the space charge limitation and becomes space charge free as a result of more balanced charge transport (25, 26).

4. CONCLUSION

In summary, we have successfully synthesized a trithiophene-bound dye, **FT**, which undergoes excited-state intramolecular proton transfer, resulting in a large Stokes shifted (9695 cm^{-1}) tautomer emission. Upon blending, efficient energy transfer from **FT** tautomer emission to **P3HT** has been proven via the associated relaxation dynamics. In **BHJ** application, blending **P3HT-PCBM** with **FT** enhances the interaction among **RR-P3HT** chains and/or between **RR-P3HT** and **PCBM**, resulting in the improvement of morphology. Among a series of devices prepared, **B-FT2** gives rise to a consistent enhancement on the efficiency, η, by a factor of 16% (c.f. **B**). Two mechanisms for the **FT** enhancing **P3HT-PCBM** solar cell are thus proposed: (1) Because of the increase in absorption in wavelengths of 360−440 nm, the **FT** addition results in more efficient light harvesting, and followed by the energy transfer from the proton-transfer form of **FT** to **P3HT**. (2) Introduction of **FT** to **P3HT/PCBM** blend films also improves the morphology of phase-separated structure, in particular, enhances the interaction of **P3HT** chains and the hole mobility. The combination of these two factors consequently increases the energy conversion efficiency.

Acknowledgment. This work was supported by the National Science Council and Ministry of Economic Affairs of Taiwan. We are also grateful to the National Center for High-Performance Computing for computer time and facilities.

Supporting Information Available: The absorption and PL spectra of **P3HT**, **P3HT-FT1**, **P3HT-FT2**, **P3HT-FT4**, and **P3HT-FT6**, as well as the time-dependent fluorescence decay dynamics of **FT** and **P3HT-FT2** in the solid thin film monitored at 580 nm (PDF). This material is available free of charge via the Internet at http://pubs.acs.org.

REFERENCES AND NOTES

(1) Silvestri, F.; Irwin, M. D.; Beverina, L.; Facchetti, A.; Pagani, G. A.; Marks, T. J. *J. Am. Chem. Soc.* **2008**, *130*, 17640–17641.

(2) Liu, Z.; Liu, Q.; Huang, Y.; Ma, Y.; Yin, S.; Zhang, X.; Sun, W.; Chen, Y. *Adv. Mater.* **2008**, *20*, 3924–3930.

(3) Yip, H. L.; Hau, S. K.; Baek, N. S.; Ma, H.; Jen, A. K. Y. *Adv. Mater.* **2008**, *20*, 2376–2382.

(4) Peet, J.; Kim, J. Y.; Coates, N. E.; Ma, W. L.; Moses, D.; Heeger, A. J.; Bazan, G. C. *Nat. Mater.* **2007**, *6*, 497–500.

(5) Walker, B.; Tamayo, A. B.; Dang, X. D.; Zalar, P.; Seo, J. H.; Garcia, A.; Tantiwiwat, M.; Nguyen, T. Q. *Adv. Funct. Mater.* **2009**, *19*, 3063–3069.

(6) Walker, B.; Tamayo, A. B.; Dang, X. D.; Zalar, P.; Seo, J. H.; Garcia, A.; Tantiwiwat, M.; Nguyen, T. Q. *Adv. Funct. Mater.* **2009**, *19*, 3063–3069.

(7) Kim, Y.; Cook, S.; Tuladhar, S.; Choulis, S. A.; Nelson, J.; Durrant, J. R.; Bradley, D. D. C.; Giles, M.; Mcculloch, I.; Ha, C.-S.; Ree, M. *Nat. Mater.* **2006**, *5*, 197–203.

(8) (a) Padinger, F.; Rittberger, R. S.; Sariciftci, N. S. *Adv. Funct. Mater.* **2003**, *13*, 85–88. (b) Li, G.; Shrotriya, V.; Yao, Y.; Yang, Y. *J. Appl. Phys.* **2005**, *98*, 043704. (c) Ma, W.; Yang, C.; Gong, X.; Lee, K.; Heeger, A. J. *Adv. Funct. Mater.* **2005**, *15*, 1617–1622. (d) Kim, Y.; Choulis, S. A.; Nelson, J.; Bradley, D. D. C.; Cook, S.; Durrant, J. R. *Appl. Phys. Lett.* **2005**, *86*, 063–502. (e) Li, G.; Yao, Y.; Yang, H.; Shrotriya, V.; Yang, G.; Yang, Y. *Adv. Funct. Mater.* **2007**, *17*, 1636–1644.

(9) Schilinsky, P.; Asawapirom, U.; Scherf, U.; Biele, M.; Brabec, C. J. *Chem. Mater.* **2005**, *17*, 2175–2180.

(10) (a) Yamamoto, T.; Komarudin, D.; Arai, M.; Lee, B.-L.; Suganuma, H.; Asakawa, N.; Inoue, Y.; Kubota, K.; Sasaki, S.; Fukuda, T.; Matsuda, H. *J. Am. Chem. Soc.* **1998**, *120*, 2047–2058. (b) Sirringhaus, H.; Brown, P. J.; Friend, R. H.; Nielsen, M. M.; Bechgaard, K.; Langeveld-Voss, B. M. W.; Spiering, A. J. H.; Janssen, R. A. J.; Meijer, E. W.; Herwig, P.; de Leeuw, D. M. *Nature* **1999**, *401*, 685–688.

(11) McCulloch, I.; Heeney, M.; Bailey, C.; Genevicius, K.; Macdonald, I.; Shkunov, M.; Sparrowe, D.; Tierney, S.; Wagner, R.; Zhang, W.; Chabinyc, M. L.; Kline, R. J.; McGehee, M. D.; Toney, M. F. *Nat. Mater.* **2006**, *5*, 328–333.

(12) Wu, I. C.; Lai, C. H.; Chen, D. Y.; Shih, C. W.; Wei, C. Y.; Ko, B. T.; Ting, C.; Chou, P. T. *J. Mater. Chem.* **2008**, *18*, 4297–4303.

(13) (a) Frey, W.; Laermer, F.; Elasesser, T. *J. Phys. Chem.* **1991**, *95*, 1039110395. (b) Schwartz, B. J.; Peteanu, L. A.; Harris, C. B. *J. Phys. Chem.* **1992**, *96*, 3591–3598. (c) Chou, P.-T.; Chen, Y.-C; Yu, W.-S.; Chou, Y.-H.; Wei, C.-Y.; Cheng, Y.-M. *J. Phys. Chem. A* **2001**, *105*, 1731–1740. (d) Paterson, M. J.; Robb, M. A; Blancafort, L.; DeBellis, A. D. *J. Am. Chem. Soc.* **2004**, *126*, 2912–2922. (e) Chen, K.-Y.; Cheng, Y.-M.; Lai, C.-H.; Hsu, C.-C.; Ho, M.-L.; Lee, G.-H.; Chou, P.-T. *J. Am. Chem. Soc.* **2007**, *129*, 4534–4535.

(14) (a) Yu, W.-S.; Cheng, C.-C.; Cheng, Y.-M.; Wu, P.-C.; Song, Y.-H.; Chi, Y.; Chou, P.-T. *J. Am. Chem. Soc.* **2003**, *125*, 10800–10801. (b) Kijak, M.; Nosenko, Y.; Singh, A.; Thummel, R. P.; Waluk, J. *J. Am. Chem. Soc.* **2007**, *129*, 2738–2739.

(15) (a) Kosower, E. M.; Huppert, D. *Annu. Rev. Phys. Chem.* **1986**, *37*, 127–156. (b) Formosinho, S. F.; Arnaut, L. G. *J. Photochem. Photobiol., A: Chem.* **1993**, *75*, 21–48. (c) Scheiner, S. *J. Phys. Chem. A.* **2000**, *104*, 5898–5909. (d) Waluk, J. *Acc. Chem. Res.* **2003**, *36*, 832–838.

(16) (a) Parsapour, F.; Kelley, D. F. *J. Phys. Chem.* **1996**, *100*, 2791–2798. (b) Sengupta, P. K.; Kasha, M. *Chem. Phys. Lett.* **1979**, *68*, 382–385. (c) Kasha, M. *J. Chem. Soc., Faraday Trans.* **1986**, *82*, 2379–2392. (d) McMorrow, D.; Kasha, M. *J. Phys. Chem.* **1984**, *88*, 2235–2243. (e) Schwartz, B. J.; Peteanu, L. A.; Harris, C. B. *J. Phys. Chem.* **1992**, *96*, 3591–3598. (f) Brucker, G. A.; Kelley, D. F. *J. Phys. Chem.* **1988**, *92*, 3805–3809.

(17) Chou, P. T.; Chen, Y. C.; Yu, W. S.; Chou, Y. H.; Wei, C. Y.; Cheng, Y. M. *J. Phys. Chem. A* **2001**, *105*, 1731–1740.

(18) Kim, K.; Carroll, D. L.; Liu, J.; Namboothiry, M. A. G. *App. Phys. Lett.* **2007**, *90*, 163511.

(19) McMorrow, D.; Kasha, M. *J. Phys. Chem.* **1984**, *88*, 2235–2243.

(20) Österbacka, R.; An, C. P.; Jiang, X. M.; Vardeny, Z. V. *Science* **2000**, *287*, 839–842.

(21) Brown, P. J.; Thomas, D. S.; Köhler, A.; Wilson, J. S.; Kim, J. S. *Phys. Rev. B* **2003**, *67*, 064203.

(22) Korovyanko, O. J.; Österbacka, R.; Jiang, X. M.; Vardeny, Z. V. *Phys. Rev. B: Condens. Matter.* **2001**, *64*, 235122.

(23) Cornil, J.; Beljonne, D.; Calbert, J. P.; Brédas, J. L. *Adv. Mater.* **2001**, *13*, 1053–1067.

(24) Brabec, C. J.; Cravino, A.; Meissner, D.; Sariciftci, N. S.; Fromherz, T.; Rispens, M. T.; Sanchez, L.; Hummelen, J. C. *Adv. Funct. Mater.* **2001**, *11*, 374–380.

(25) Olson, D. C.; Lee, Y. J.; White, M. S.; Kopidakis, N.; Shaheen, S. E.; Ginley, D. S.; Voigt, J. A.; Hsu, J. W. P. *J. Phys. Chem. C* **2007**, *111*, 16640–16645.

(26) von Hauff, E.; Parisi, J.; Dyakonov, V. *J. Appl. Phys.* **2006**, *100*, 043702.

AM100126Y